JOURNAL OF COMPUTATIONAL PHYSICS 25, 366–385 (1977)

A Numerical Algorithm for Remote Sensing of Density Profiles of a Simple Ocean Model by Acoustic Pulses

Y. M. CHEN AND D. S. TSIEN

Department of Applied Mathematics and Statistics, State University of New York at Stony Brook, Stony Brook, New York 11794

Received December 3, 1976; revised January 26, 1977

An iterative algorithm for solving nonlinear inverse problems in remote sensing of density profiles of a simple ocean model by using acoustic pulses is developed. Here the adiabatic sound velocity is assumed to be proportional to the inverse square root of the density. The basic idea of this new algorithm is that first, the original pulse problem in the time domain is reduced to a continuous wave problem in the frequency domain and then the nonlinear inverse problem in the frequency domain is solved by a hybrid of a Newton-like iterative method, Backus and Gilbert linear inversion technique, and the finite difference method. This new computational algorithm is tested by numerical simulations with given data from 10 different frequencies and is found to give excellent results. The effects of taking data from various frequency ranges and of the contaminating instrument and ambient noise on the accuracy and efficiency of numerical computation are investigated. It is found that the low frequency data are preferred over the data from the high frequency spectrum. Under favorable conditions, the maximum pointwise numerical error of the density profile $\rho(x)$ is less than 5% of the total variation of the density profile,

$$\rho_{tv} \equiv |\operatorname{Max} \rho(x) - \operatorname{Min} \rho(x)|.$$

Better result can be achieved if a large number of data are available and more efforts are made in the numerical computation.

INTRODUCTION

Ocean density profiles can be computed from a finite number of experimental data obtained through acoustic remote sensing techniques as opposed to *in situ* measurement. Often these types of remote sensing problems can be formulated as "improperly posed" linear or nonlinear inverse problems of partial differential equations in mathematical analysis, and usually the solution of an inverse problem is not unique and does not depend continuously on the given data. To solve linear or nonlinear inverse problems is equivalent to constructing approximate solutions of linear or nonlinear operator equations from inadequate data with or without statistical measurement errors. While the computational methods for solving the traditional direct problems of partial differential equations, e.g., the finite difference method, the finite element method, their hybrids, etc., are quiet well developed, the numerical

ISSN 0021-9991

methods for solving inverse problems are still in their infancies. Hence the need of new developments in the computational methods for solving inverse problems is definitely in order.

Recently, several iterative algorithms for solving inverse problems of nonlinear operator equations in Banach spaces have been developed by Chen and Surmont [1, 2], and they have been used for solving a nonlinear radiative transfer problem in the remote sensing of atmospheric temperature profiles [3]. These algorithms are basically hybrids of Newton's iterative methods in Banach spaces [4] and the linear inversion technique of Backus and Gilbert (B & G) [5–7]. Of course, many other linear inversion techniques, e.g., the regularization method of Tihonov [8], the Moore–Penrose pseudoinverse method [9], etc., can be used just the same. But, the B & G method is preferred here for the reason that it not only provides an inversion tehcnique, but also can be used as a diagnostic tool for testing the intrinsic resolution of a given set of data for a given problem (or mathematically, provides a sort of pointwise error estimates). More recently, Tsien and Chen [10] has introduced a hybrid of the above-mentioned iterative algorithms and the finite difference method to infer the ocean density profiles by using low frequency acoustic continuous wave (CW) measurements with success; the frequency range is such that the ocean depth is in the range of one to four wavelengths.

Now, a numerical algorithm for solving the nonlinear inverse problem in remote sensing of density profiles of a simple ocean model by using acoustic pulses is developed in this paper. Here the adiabatic sound velocity is assumed to be proportional to the inverse square root of the density function. The basic idea of this algorithm is that the incident and reflected acoustic pulses are assumed to be known at the surface of the ocean; through Fourier sine or cosine transform with respect to time t, the original pulse problem in time domain is reduced to a CW problem in frequency domain. Hence the numerical method of [10] can be applied. This new computational algorithm is tested by numerical simulation and it is found to give excellent results. The effects of taking data from various ranges of the frequency spectrum as the input to the numerical algorithm on the accuracy and efficiency of computations are thoroughly studied; the entire frequency range is such that the ocean depth is in the range of 1 to 320 wavelengths. Moreover, the effects of the contaminating instrument and ambient noise on the accuracy of the numerical results or the intrinsic resolution of a given set of measured data are carefully investigated. Finally, a comprehensive discussion of the numerical results and their implication in actually implementing this computational algorithm is given.

It should be pointed out that there are two basic differences between the new numerical algorithm here and the conventional approach [11–18] for solving inverse Sturm–Liouville problems. First, a precise knowledge of complete sets of eigenvalues of a particular Sturm–Liouville problem and its associated problems is needed to solve the inverse problem uniquely in the conventional approach, but no such knowledge is needed in the new numerical algorithm here. As a matter of fact, here the choice of the discrete values in frequency domain $\{\omega_i\}$, $i = 1, 2, \ldots, I$ (not the square roots of the eigenvalues) is completely arbitrary. Hence they can be chosen for practical and

computational conveniences. Second, the concept of the uniqueness of solutions, which is a major concern in the conventional approach, is replaced here by a weaker but more practical one, "the closeness of different numerical solutions to a solution." In the new numerical algorithm here, each iterative calculation with different initial iterate will converge to a different but unique numerical solution [2]; nevertheless this nonuniqueness poses no real difficulty for practical problems. If several different numerical solutions are all close enough to the exact solution, then in practical sense any one of them will be an acceptable good solution. Hence in the new numerical algorithm here, the major concern is the closeness of different numerical solutions to the exact solution. In general, the "closeness" is characterized qualitatively by the "spread of the averaging kernel," i.e., the smaller the spread, the closer is the numerical solution to the actual solution. This is because the "spread" characterizes the "closeness" of the numerical solutions of the individual interate linearized problem and the new numerical algorithm here can be shown to be a Newton-like iterative method whose accuracy is in direct proportion to the numerical accuracy in computing the individual iterate [2]. The "spread" is a by-product in the process of computing the numerical solution. The quantitative information on the closeness can be obtained by performing simple numerical simulations.

Formulation of the Problem

The hydrodynamic structure of the ocean is assumed to be a compressible, inviscous, and stratified fluid layer above a rigid plane (Fig. 1). The linearized governing equations in remote sensing of ocean density profiles by using acoustic pulses are [19]

$$\begin{aligned} \partial u/\partial t &= -\rho^{-1}\,\partial p/\partial x, \qquad 0 < x < H, \\ \partial p/\partial t &= -\rho c^2\,\partial u/\partial x, \qquad 0 < t, \end{aligned} \tag{1}$$

with initial conditions

$$\begin{aligned} u(x, 0) &= 0, \\ p(x, 0) &= 0, \end{aligned} \tag{2}$$

and boundary conditions

$$\begin{aligned} u(H, t) &= 0, \\ p(0, t) &= f(t), \end{aligned} \tag{3}$$

where p is the pressure, u is the particle velocity, ρ is the equilibrium density, c is the adiabatic sound velocity related to ρ through the known equation of state $c = (\rho K)^{-1/2}$ [20], K is the compressibility coefficient which is assumed to be constant,

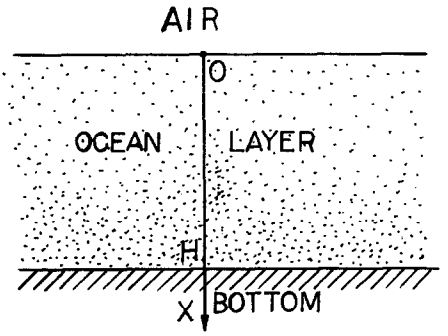

FIG. 1. Ocean layer with a rigid bottom.

and $f(t)$ is a pulse function with a given duration which corresponds to the incident pulse.

The mathematical problem in remote sensing of ocean density profiles is to determine the density function from Eqs. (1)–(3) and $\partial p/\partial x\,|_{x=0}$. To transform the above-mentioned pulse problem in the time domain to its corresponding CW problem in the frequency domain, the Fourier transform with respect to t is needed. In particular, due to the homogeneous initial conditions the Fourier sine transform is applied to Eqs. (1)–(3). Upon eliminating the Fourier sine transform of u, Eqs. (1)–(3) lead to a Sturm–Liouville type of ordinary differential equation for $\mathbf{p}(x, \omega)$, the Fourier sine transform of p,

$$\begin{aligned} d/dx\,(\rho^{-1}\,d\mathbf{p}/dx) + \omega^2 K\mathbf{p} &= 0, \\ \mathbf{p}(0, \omega) &= \mathbf{f}(\omega), \\ d\mathbf{p}(x, \omega)/dx\,|_{x=H} &= 0, \end{aligned} \tag{4}$$

where $\mathbf{f}(\omega)$ is the Fourier sine transform of $f(t)$ and ω is the angular frequency.

Upon normalizing K to unity and introducing the dimensionless variables, $x' = x/H$, $\mathbf{p}' = \mathbf{p}/\mathbf{f}(\omega)$, $\rho' = \rho/\rho(0)$, and $\omega' = \omega H/c(0)$, Eq. (4) becomes

$$\begin{aligned} d/dx\,(\rho^{-1}\,d\mathbf{p}/dx) + \omega^2\mathbf{p} &= 0, \\ \mathbf{p}(0, \omega) &= 1, \\ d\mathbf{p}(x, \omega)/dx\,|_{x=1} &= 0, \end{aligned} \tag{5}$$

where $\rho(0)$ and $c(0)$ are the values of $\rho(x)$ and $c(x)$ at $x = 0$ and they are assumed to be known. Here the primes are dropped for convenience.

Now, the inverse problem is to determine $\rho(x)$ from (5) and the known values of $d\mathbf{p}(0, \omega)/dx$ for a set of $\{\omega_i\}$, $i = 1, 2, \ldots, I$. Although Eq. (5) is a linear ordinary differential equation, the inverse problem is nonlinear in nature.

NUMERICAL ALGORITHM

In general, a nonlinear inverse problem can be solved by using the iterative algorithms of [1–3]. For the nonlinear inverse problem here, a variant of the above-mentioned iterative algorithms is used and it is presented in the following.

Let

$$\mathbf{p}_{n+1} = \mathbf{p}_n + \delta\mathbf{p}_n, \qquad \rho_{n+1} = \rho_n + \delta\rho_n, \qquad n = 0, 1, 2,... \tag{6}$$

be the $(n+1)$th iterates of $\mathbf{p}$ and ρ such that $|\delta\mathbf{p}_n| < |\mathbf{p}_n|$, $|\delta p_n| < |\rho_n|$, and $\delta p_n(0) = 0$. The $\mathbf{p}_0$ and ρ_0 are the initial guess. Upon substituting (6) into (5) and neglecting terms of $O\{(\delta\mathbf{p}_n)^2\}$, $O\{(\delta\rho_n)^2\}$ and higher, one obtains

$$\begin{aligned} &d/dx(\rho_n^{-1}\, d\mathbf{p}_n/dx) + \omega^2\mathbf{p}_n = 0, \\ &\mathbf{p}_n(0, \omega) = 1, \qquad d\mathbf{p}_n(x, \omega)/dx\,|_{x=1} = 0, \end{aligned} \tag{7}$$

and

$$\begin{aligned} &d/dx(\rho_n^{-1}\, d\delta\mathbf{p}_n/dx) + \omega^2\,\delta\mathbf{p}_n = d/dx(\rho_n^{-2}\,\delta\rho_n\, d\mathbf{p}_n/dx), \\ &\mathbf{p}_n(0, \omega) = 0, \qquad d\delta\mathbf{p}_n(x, \omega)/dx\,|_{x=1} = 0. \end{aligned} \tag{8}$$

By using the method of Green's function [21], after a considerable amount of manipulation one obtains a Fredholm integral equation of the first kind which relates $\rho_n(x)$ to $d\,\delta\mathbf{p}_n(x, \omega)/dx\,|_{x=0}$,

$$\int_0^1 \{\rho_n^{-1}(x')\, d\mathbf{p}_n(x', \omega)/dx'\}^2\,\delta\rho_n(x')\, dx' = d\delta\mathbf{p}_n(x, \omega)/dx\,|_{x=0}. \tag{9}$$

Now the inverse problem is reduced to for each iteration the determination of $\delta\rho_n(x)$ from a set of measured data $\{d\,\delta\mathbf{p}(0, \omega_i)/dx\}$, $i = 1, 2, 3,..., I$. These measured data are used as the input data to the right-hand side of Eq. (9) for the purpose of accelerating the rate of convergence. This inverse problem can be solved by the linear inversion technique of B & G [5–7]. It starts with

$$\delta\rho_n(x) = \sum_{i=1}^{I} a_{in}(x)\, d\delta\mathbf{p}(0, \omega_i)/dx. \tag{10}$$

Upon substituting Eq. (10) into Eq. (9), one obtains the integral expression,

$$\delta\rho_n(x) = \int_0^1 A_n(x, x')\,\delta\rho_n(x')\, dx', \tag{11}$$

where

$$A_n(x, x') = \sum_{i=1}^{I} a_{in}(x)\,\{p_n^{-1}(x')\, d\mathbf{p}_n(x', \omega_i)/dx'\}^2, \tag{12}$$

is known as the "averaging kernel" and is subjected to the normalization condition,

$$\int_0^1 A_n(x, x')\, dx' = 1. \tag{13}$$

The "spread of A_n from x" is defined by

$$Q_n(x, A_n) \equiv 12 \int_0^1 (x - x')^2 A_n^2(x, x')\, dx'. \tag{14}$$

If the measured data are errorless, the set of unknown functions $\{a_{in}(x)\}$, $i = 1, 2, 3, \ldots, I$, should be chosen such that the averaging kernel A_n resembles the Dirac delta function $\delta(x' - x)$ most closely, or equivalently, the positive-definite quadratic form of $\{a_{in}(x)\}$, $i = 1, 2, 3, \ldots, I$, $Q_n(x, A_n)$ is minimized subject to the constraint (13). Hence the method of Lagrange multipliers is used.

If the measured data contain errors, then the variance of the density error $\sigma_n^2(x)$ incurred at x due to random measurement errors can be found from Eq. (10) to be

$$\sigma_n^2(x) = \tilde{A}_n(x) \cdot \tilde{E} \cdot \tilde{A}_n(x), \tag{15}$$

where the vector $\tilde{A}_n(x) \equiv \{a_{in}(x)\}$, $i = 1, 2, 3, \ldots, I$, $\tilde{E}$ is the covariance tensor for the random errors of $\{d\mathbf{p}(0, \omega_i)/dx\}$, $i = 1, 2, 3, \ldots, I$, and the means of the random errors are assumed to be zero.

Ideally, one would like to be able to choose $\tilde{A}_n(x)$ such that both $\sigma_n^2(x)$ and $Q_n(x, A_n)$ are minimized. However, this cannot be done, but it is possible to minimize a linear combination of $\sigma_n^2(x)$ and $Q_n(x, A_n)$,

$$G_n \equiv (1 - s)\, Q_n(x, A_n) + s\sigma_n^2(x). \tag{16}$$

By varying the parameter s between zero and unity, the emphasis can be shifted from minimization of the spread to minimization of the error. Thus, there is a trade-off between intrinsic resolution and the accuracy in the presence of measurement errors. The best choice for s must be determined by the particular problem.

Now, for a given value of s the minimization of G_n subject to the constraint Eq. (13) gives

$$\tilde{A}_n(x) = \tilde{W}_n^{-1}(x) \cdot \tilde{B}_n / \tilde{B}_n \cdot \tilde{W}_n^{-1}(x) \cdot \tilde{B}_n\,, \tag{17}$$

where the matrix $\tilde{W}_n(x)$ is defined by

$$\tilde{W}_n(x) = (1 - s)\tilde{Q}_n(x) + s\tilde{E} \tag{18}$$

with the elements of $\tilde{Q}_n(x)$,

$$q_{iin}(x) = 12 \int_0^1 (x - x')^2 \{\rho_n^{-1}(x')\, d\mathbf{p}_n(x', \omega_i)/dx'\}^2 \cdot \{\rho_n^{-1}(x')\, d\mathbf{p}_n(x' \cdot \omega_j)/dx'\}^2\, dx', \quad i, j = 1, 2, 3, \ldots, I \tag{19}$$

and the components of $\tilde{B}_n$,

$$b_{in} = \int_0^1 \{\rho_n^{-1}(x')\, d\mathbf{p}_n(x', \omega_i)/dx'\}^2\, dx', \qquad i = 1, 2, 3, \ldots, I. \tag{20}$$

Finally for each iterate, once $\tilde{A}_n(x)$ is known from Eq. (17), $\delta\rho_n(x)$ can be calculated from Eq. (10).

Procedure for Numerical Simulation

In order to test the feasibility and to study the general characteristics of the new computational algorithm without the real measurement data, a numerical simulation must be carried out. The procedure is:

(I) First, a typical density profile of the ocean [20] $\rho^*(x)$ is assumed to be the correct density function. The corresponding pressures $\{\mathbf{p}^*(x, \omega_i)\}$ are obtained from Eq. (5) for a set of angular frequencies $\{\omega_i\}$, $i = 1, 2, 3, \ldots, I$, by solving the two-point boundary value problem. Then by a finite difference approximation, $\{d\mathbf{p}^*(0, \omega_i)/dx\}$, $i = 1, 2, 3, \ldots, I$, are obtained as the equivalence of the measured data.

(II) The measurement errors can be simulated by multiplying the data, $\{d\mathbf{p}^*(0, \omega_i)/dx\}$, $i = 1, 2, 3, \ldots, I$, by corresponding factors, $\{(1 + kR_i)\}$, $i = 1, 2, 3, \ldots, I$, where k is the amplitude factor ($k = 0.001$ used here) and R_i's are the random numbers generated by a random number generator subroutine [22].

(III) Next, $\rho_0(x)$ is assumed. Then $\{\mathbf{p}_0(x, \omega_i)\}$ and $\{d\mathbf{p}_0(0, \omega_i)/dx\}$, $i = 1, 2, 3, \ldots, I$, are determined from Eq. (7) by using the same numerical methods as those of of Step I. Next, the nonhomogeneous term of Eq. (9) can be computed as $d\,\delta\mathbf{p}_0(0, \omega_i)/dx = (1 + kR_i)\, d\mathbf{p}^*(0, \omega_i)/dx - d\mathbf{p}_0(0, \omega_i)/dx$.

(IV) Finally, $\delta\rho_0(x)$ is obtained from Eq. (9) and the data $\{d\,\delta\mathbf{p}_0(0, \omega_i)/dx\}$, $i = 1, 2, 3, \ldots, I$, by using the linear inversion technique of B & G [5–7], described in the previous section. Hence from Eq. (6), $\rho_1(x)$ is obtained.

Other than the truncation, round-off, and numerical integration errors, the L_2 norm $\| \rho^*(x) - \rho_n(x) \|$ can be used as a criterion for evaluating the performance of the numerical algorithm consisting of Steps III and IV. Although only continuous functions are considered, the L_2 norm is used here because of its integrated effect. If the desired accuracy is not met, then one can repeat Steps III and IV until the desired accuracy is achieved. The proof of the convergence of this iteration method will be shown elsewhere.

Steps I and III involve solutions of the two-point boundary value problem of the Sturm–Liouville type of ordinary differential equations. In general, a two-point boundary value problem can be solved by using shooting methods [23] with the help of a sophisticated ordinary differential equations solver, GEAR algorithm [24, 25].

However, in the range of $\omega = 1$ to $\omega = 30$, the GEAR algorithm is not as efficient as the simpler finite difference method with second order accuracy, e.g., the center difference approximation. In the range of $\omega \geqslant 1000$ where the oscillation of the solution is extremely high, again the GEAR algorithm becomes inefficient. It is easier to obtain the asymptotic solution of the two-point boundary value problem by using the WKBJ method [26, 27] (Appendix A).

Numerical Results with Errorless Data

Numerical simulations are carried out for several $\rho_0(x)$ with errorless data in the range of angular frequency, $5 \leqslant \omega \leqslant 2000$. In performing Step IV, Simpson's rule is used in the numerical integration. The numerical results and their relevant

TABLE I

Squares of Norms are Expressed in Units of 10^{-8}

Fig.	$\{\omega_i'\}$	$\rho_0'(x')$	n, No. of Iteration	Method used in Steps I & III	$\|\rho'^* - \rho_n'\|^2$
2	6.98, 8.72, 10.12, 11.86, 13.26, 15.00, 16.40, 18.14, 19.54, 21.28	Smooth, $\|\rho'^* - \rho_0'\|^2 = 15.175$	3	Implicit finite difference $\Delta x' = 0.00625$	2.1802
3	Same as above	Zigzag, $\|\rho'^* - \rho_0'\|^2 = 100.13$	4	Same as above	8.9106
4	Same as above	Smooth, $\|\rho'^* - \rho_0'\|^2 = 1340.4$	2	Same as above	10.009
5	100, 110, 120, 130, 140, 150, 160, 170, 180, 190	Same as above	2	Shooting method, "GEAR"	23.121
6	210, 215, 220, 225, 230, 310, 315, 320, 325, 330	Same as above	2	Same as above	25.660
7	410, 415, 420, 425, 430, 435, 440, 445, 450, 455	Same as above	2	Same as above	54.434
8	10, 20, 30, 40, 50, 460, 550, 640, 730, 820	Same as above	2	Same as above	21.241
9	1100, 1200, 1300, 1400, 1500, 1600, 1700, 1800, 1900, 2000	Same as above	2	WKBJ method	601.92

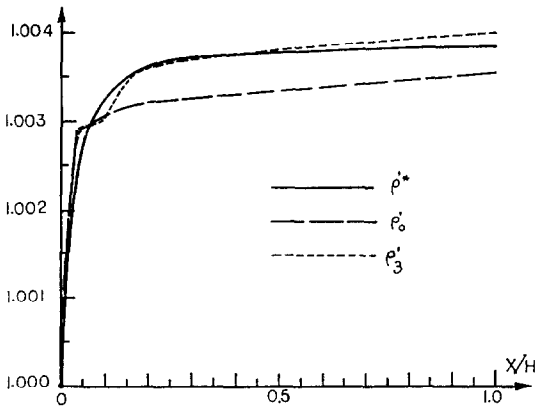

FIG. 2. Comparison of the calculated and the exact normalized density profiles, with smooth $\rho_0'(x')$, small $\| \rho'^* - \rho_0' \|$, and errorless data in $6.5 < \omega' < 21.5$.

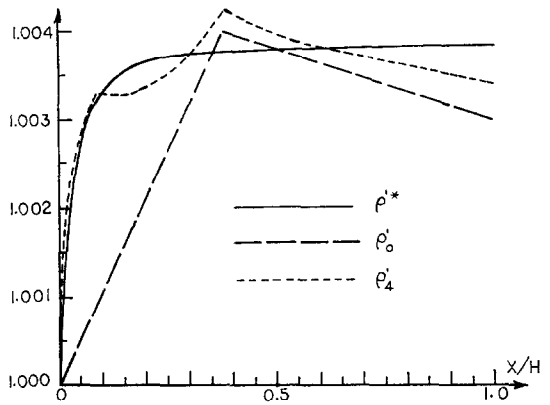

FIG. 3. Comparison of the calculated and the exact normalized density profiles, with zigzag $\rho_0'(x')$, small $\| \rho'^* - \rho_0' \|$, and errorless data in $6.5 < \omega' < 21.5$.

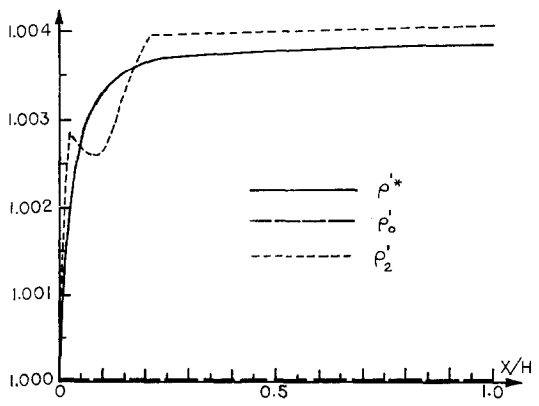

FIG. 4. Comparison of the calculated and the exact normalized density profiles, with smooth $\rho_0'(x')$, large $\| \rho'^* - \rho_0' \|$, and errorless data in $6.5 < \omega' < 21.5$.

information are given in Table I and Figs. 2–9. Three typical oscillatory $\{\rho_n^{-1}(x)\, d\mathbf{p}_n(x, \omega_i)/dx\}^2$ are plotted in Fig. 10. The averaging kernels $A(x_0, x)$ at four different x_0 are shown in Fig. 11. The primes of the independent and dependent variables are reinstalled in all tables and figures.

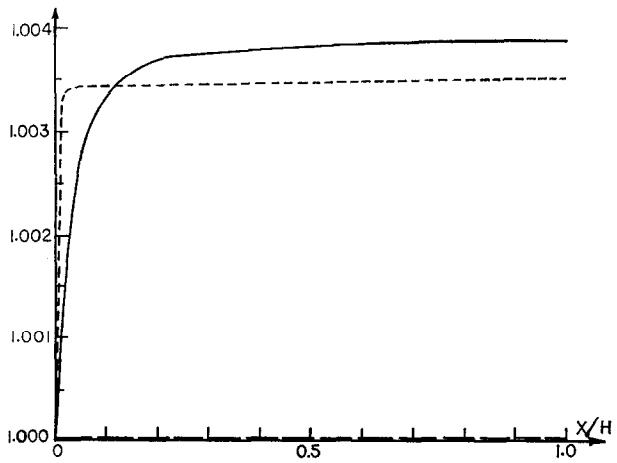

FIG. 5. Comparison of the calculated and the exact normalized density profiles, with smooth $\rho_0'(x')$, large $\|\rho'^* - \rho_0'\|$, and errorless data in $100 \leqslant \omega' \leqslant 190$: ——— ρ'^*; — — — ρ_0'; - - - - ρ_2'.

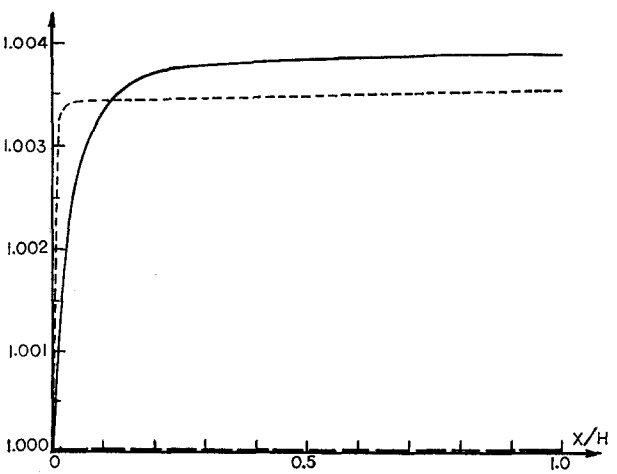

FIG. 6. Comparison of the calculated and the exact normalized density profiles, with smooth $\rho_0'(x')$, large $\|\rho'^* - \rho_0'\|$, and errorless data in $210 \leqslant \omega' \leqslant 330$: ——— ρ'^*; — — — ρ_0'; - - - - ρ_2'.

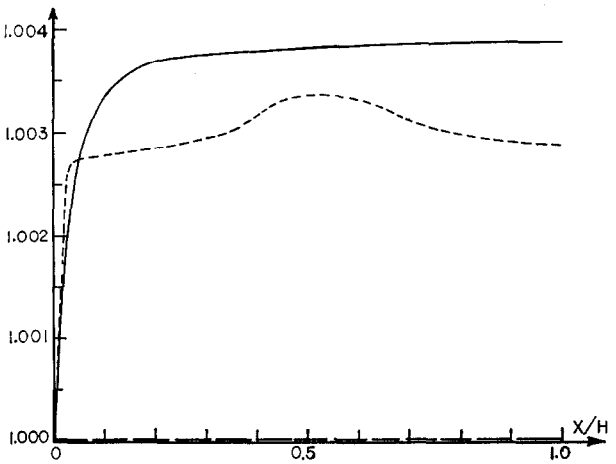

FIG. 7. Comparison of the calculated and the exact normalized density profiles, with smooth $\rho_0'(x')$, large $\| \rho'^* - \rho_0' \|$, and errorless data in $410 \leqslant \omega' \leqslant 455$: ——— ρ'^*; — — — ρ_0'; - - - - ρ_2'.

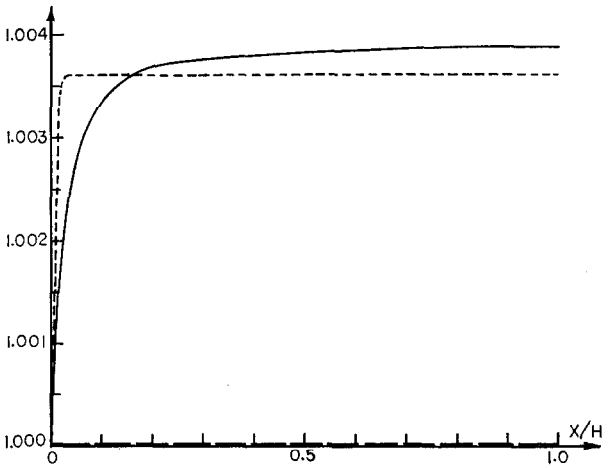

FIG. 8. Comparison of the calculated and the exact normalized density profiles, with smooth $\rho_0'(x')$, large $\| \rho'^* - \rho_0' \|$, and errorless data in $10 \leqslant \omega' = 820$: ——— ρ'^*; — — — ρ_0'; - - - - ρ_2'.

NUMERICAL RESULTS WITH ERRONEOUS DATA

In this section, the effects of the contaminating instrument and ambient noise on the accuracy of the numerical results or the intrinsic resolution of a given set of measured data are studied. The measurement errors are simulated by the procedure

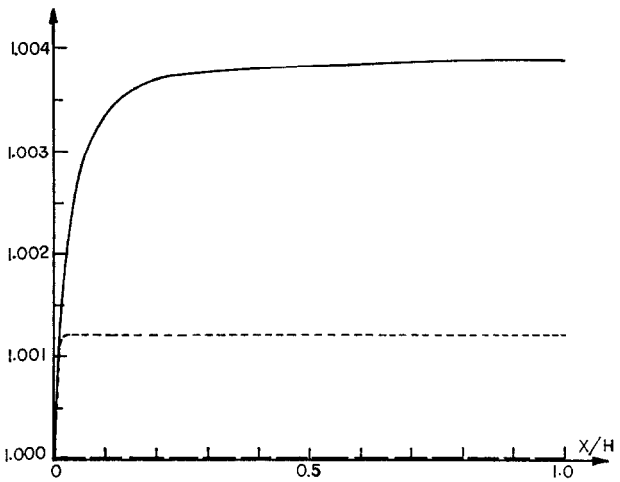

FIG. 9. Comparison of the calculated and the exact normalized density profiles, with smooth $\rho_0'(x')$, large $\|\rho'^* - \rho_0'\|$, and errorless data in $1100 \leqslant \omega' \leqslant 2000$; ——— ρ'^*; — — — ρ_0'; - - - - ρ_2'.

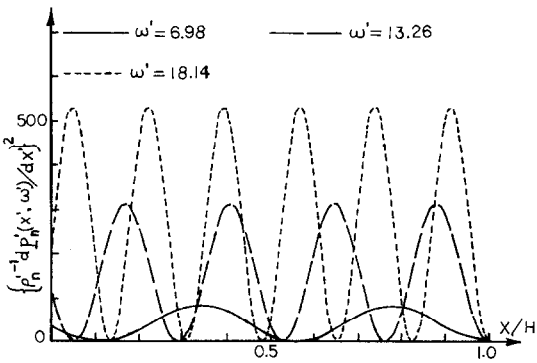

FIG. 10. Typical $\{\rho'^{-1}(x')\, d\mathbf{p}_n'(x', \omega')/dx'\}^2$ as function of x' shown for three different values of ω'.

described in Step II. The covariance tensor of the measurement errors $\tilde{E}$ is assumed to be a diagonal matrix with elements

$$e_{ii} = \{0.001 R_i\, d\mathbf{p}^*(0, \omega_i)/dx\}^2, \qquad i = 1, 2, 3, \ldots, I. \tag{21}$$

Consistent with the study of the effects of errorless data from various ranges of the frequency spectrum on the accuracy of the numerical results in the previous section, the example of Fig. 4 is used for the study here. The effect of the weight parameter s on the accuracy of the numerical result is shown in Fig. 12 and the numerical result $\rho_2(x)$ for the case $s = 0$ is plotted in Fig. 13. The trade-off curves (σ_2 vs s curves) for many ocean depths $x_1 = 0.00625$, $x_2 = 0.10625$, $x_3 = 0.20625$, $x_4 = 0.30625$,

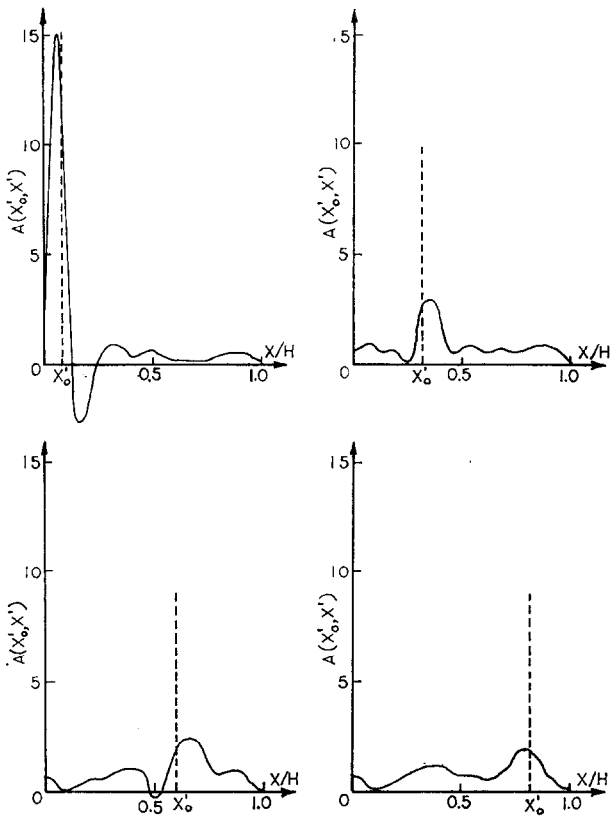

FIG. 11. Typical averaging kernel $A(x_0', x')$ as function of x' shown for four different x_0' with errorless data in $6.5 < \omega' < 21.5$.

$x_5 = 0.40625$, $x_6 = 0.50625$, $x_7 = 0.60625$, $x_8 = 0.70625$, $x_9 = 0.80625$, $x_{10} = 0.90625$ are shown in Fig. 14. Finally, the averaging kernels corresponding to $s = 0$ at four different ocean depths are plotted in Fig. 15. Again the primes of the independent and dependent variables are reinstalled in all figures.

DISCUSSION

For the case of errorless data, all of the numerical results in Table I and Figs. 2–9 indicate that our numerical algorithm has better resolution near the ocean surface than that near the ocean bottom, i.e., the numerical solutions in general are more accurate in the upper region of the ocean than other regions. This conclusion can also be drawn by carefully examining the averaging kernels in Fig. 11 where the averaging kernels resemble the Dirac delta function most near the ocean surface.

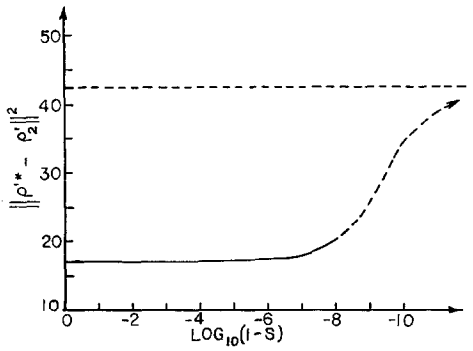

FIG. 12. With erroneous data in $6.5 < \omega' < 21.5$, the numerical error of the example in Fig. 4, characterized by $\| \rho'^* - \rho_2' \|^2$, shown to be a monotonic increasing function of s.

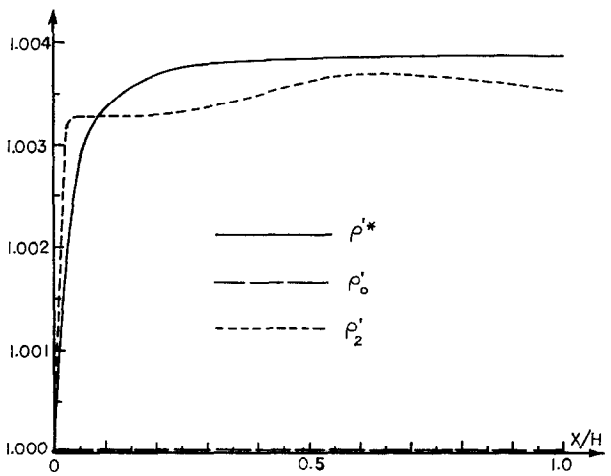

FIG. 13. Comparison of the calculated and the exact normalized density profiles of the example in Fig. 4 with erroneous data in $6.5 < \omega' < 21.5$ and $s = 0$.

The numerical results in Table I and Figs. 2–4 suggest that the closer the initial guess $\rho_0(x)$ to the exact solution $\rho^*(x)$, the more accurate the numerical solution will be. However, it can be shown that due to the smallness of the number (inadequate) of data, the limit of the iterates differs from the exact solution and depends on the initial iterate. The detail of this has been discussed in [2]. Hence in the real computation, the initial guess should be made as close to the exact profile as possible.

The numerical results in Table I and Figs. 4–9 exhibit the fact that data from lower frequency ranges give better numerical accuracy than those from higher frequency ranges. This outcome is not surprising at all, because in Steps I and III of our numerical simulations the ordinary differential equations solvers used here are inefficient in the high frequency range. At the same time, in Step IV of our numerical simulations the

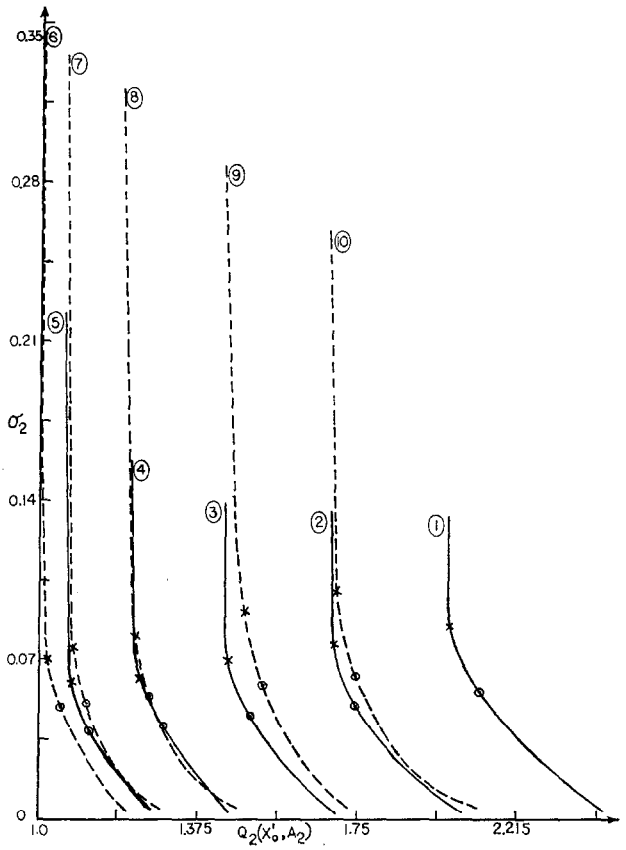

FIG. 14. With erroneous data in $6.5 < \omega' < 21.5$, trade-off curves 1, 2, 3,..., and 10 corresponding to $x_0' = 0.00625$, 0.10625, 0.20625, 0.30625, 0.40625, 0.50625, 0.60625, 0.70625, 0.80625, and 0.90625, respectively, one shown. The top and bottom end points correspond to $s = 0$ and $s = 1$, respectively. x denotes $s = 1 - 10^{-7}$ and $\odot$ denotes $s = 1 - 0.5 \times 10^{-7}$.

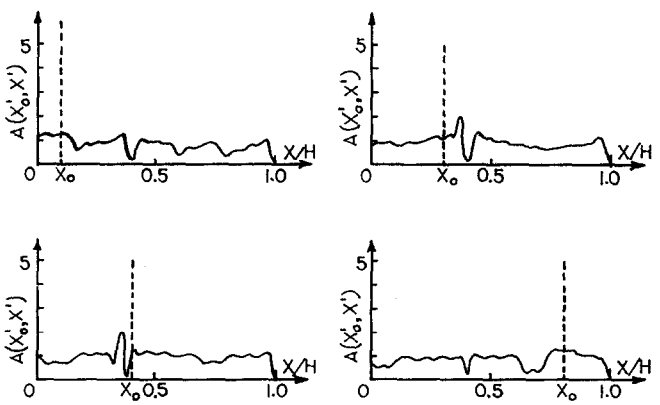

FIG. 15. Typical averaging kernel as a function of x' shown for four different x_0' with erroneous data in $6.5 < \omega' < 21.5$ and $s = 0$.

kernel of the Fredholm integral equation of the first kind Eq. (9) is much less oscillatory in the lower frequency range than that in the higher frequency range (Fig. 10). This means that the numerical solution of Eq. (9) obtained by using the same size of the integration subinterval Δx and the same quadrature formula is more accurate in the lower frequency range than in the higher frequency range; large reduction of the size of Δx for the case of high frequency will not only make the quadrature formula more inefficient but also will increase greatly the globe round-off error in the numerical computation. Hence in actual computation, low frequency data are much more preferred than those in high frequency range. Moreover, there are several other advantages for using data from the low frequency range and they will be discussed later.

For the case of erroneous data, Fig. 12 shows that the accuracy of the numerical result decreases as the parameter s increases. Even when $s = 0$ (Fig. 13) corresponding to the minimization of the spread alone, the accuracy is poorer than the analogous case with errorless data. This means that no matter how small the contaminating instrument and ambient noise can be, they will lower the performance of the numerical algorithm.

The gross behavior of the trade-off curves (Fig. 14) is the same for all x. The random error decreases monotonically with increasing spread. The decrease is rapid at small values of the spread, followed by a rather abrupt leveling off with increasing spread. The end point of the curve corresponding to minimum spread and maximum random error corresponds to $s = 0$ while the opposite end of the curve corresponds to $s = 1$. In actual computation, a happy compromising choice of s is in the range of s corresponding to the neighborhood of the bottom of the steep portion of the trade-off curves ($0.5 \lesssim (1 - s) \cdot 10^7 \lesssim 1$). In this way, the effect of random error is almost minimized, while the spread is also near its minimum. Moreover, upon examining the trade-off curves for different x, one finds that contrary to the case of errorless data where the numerical algorithm has the best resolution near the top of the ocean layer, the random errors in the data have shifted the maximum resolution of the numerical algorithm to somewhere in the middle of the ocean layer. This fact has been born out also from the study of the averaging kernels for different x in Fig. 15.

In the real situation, there are three major reasons for favoring the use of the low frequency data (other than the accuracy of the numerical algorithm). First, the low frequency component acoustic waves are less sensitive to the ocean bottom irregularities and other scattering marine objects than the high frequency component waves. For example, if the ocean depth is 5000 m and the average sound velocity is 1500 m/sec, then the normalized angular frequency range $5 \leqslant \omega' \leqslant 50$ corresponds to the real frequency range $0.239 \leqslant f \leqslant 2.387$ Hz with wavelength λ in the range $628 \leqslant \lambda \leqslant 6284$ m. Hence it is conservative to say that our numerical algorithm with measured data in the above-mentioned low frequency range will not be sensitive to any irregularity with size less than 500 m.

Second, the low frequency component acoustic waves experience less damping due to viscosity than the high frequency waves when propagating through a fixed distance in the ocean, so the received reflected signals will not be drowned out by the contaminating instrument and ambient noise.

Third, low frequency components of both incident and reflected acoustic pulses contain more energy than the high frequency components. Hence in practice, the adverse effects of the contaminating instrument and ambient noise are minimized. To justify the statement about the spectral energy, a numerical simulation of a short acoustic pulse propagating through an ocean layer with the exact density profile $\rho^*(x)$ is performed in Appendix B. This third advantage of low over high frequencies can be overcome by proper choice of hardware designs, e.g., transducers.

TABLE II

Fig.	$\text{Max}_{0\leqslant x\leqslant H} \mid \rho^*(x) - \rho_0(x)\mid$	$\text{Max}_{0\leqslant x\leqslant H} \mid \rho^*(x) - \rho_n(x)\mid$	Data
2	$0.13\ \rho_{tv}$	$0.05\ \rho_{tv}$	Errorless
3	$0.64\ \rho_{tv}$	$0.13\ \rho_{tv}$	Errorless
4	$1.00\ \rho_{tv}$	$0.16\ \rho_{tv}$	Errorless
13	$1.00\ \rho_{tv}$	$0.18\ \tau_{tv}$	With random errors

To obtain a more realistic but conservative evaluation of the performance of the numerical algorithm in this paper with data in the low refquency range, the maximum pointwise numerical error should be used as the evaluation criterion. Upon introducing the total variation of the density profile, $\rho_{tv} = \mid \text{Max}_{0\leqslant x\leqslant H}\, \rho(x) - \text{Min}_{0\leqslant x\leqslant H}\, \rho(x)\mid$, which equals $0.00385\rho(0)$ here and is less than $0.004\rho(0)$ in any real situation [20], our numerical results are given in Table II. The numerical results indicate that if the low frequency data are errorless and the initial density profile is close enough to the true profile, the maximum possible pointwise numerical error is less than 5% of the total variation of the density profile. The accuracy of the numerical algorithm can be improved greatly if there are more measured data available and improevments in the numerical accuracy are made for each individual step of the numerical algorithm. However, in this way the expense incurred in the numerical computation will be greatly increased. Hence in practice, on a priori decision on how to trade off must be made for each problem.

Appendix A

For $\omega \gg 100$, the solution of the two-point boundary value problem Eq. (7) becomes highly oscillatory. Hence the GEAR algorithm becomes inefficient. An excellent method to circumvent this difficulty is to construct the asymptotic solution of the two-point boundary value problem for large ω by using the WKBJ method [26, 27]. Again in this and the next appendix, the primes are dropped for convenience.

First, upon setting $v_n(x, \omega) = \mathbf{p}_n(x, \omega)/\rho_n^{1/2}(x)$, Eq. (7) is transformed into

$$\begin{aligned} v_n''(x, \omega) + J_n^2(x, \omega)\, v_n(x, \omega) &= 0, \\ v_n(0, \omega) &= 1, \\ v_n'(1, \omega) + \tfrac{1}{2}\rho_n^{-1}(1)\, \rho_n'(1)\, v_n(1, \omega) &= 0, \end{aligned} \tag{A.1}$$

where

$$J_n^2(x, \omega) = \tfrac{1}{2}\rho_n^{-1}(x)\, \rho_n''(x) - \tfrac{3}{4}(\rho_n^{-1}(x)\, \rho_n'(x))^2 + \rho_n(x)\omega^2 \tag{A.2}$$

and "$'$" $\equiv d/dx$. If $\rho_n(x) \neq 0$ for all x and $\rho_n''(x)$ is continuous, which is the case here, the asymptotic solution of Eq. (A.1) is given by

$$v_n(x, \omega) = J_n^{-1/2}(x, \omega)\, \{a_n(\omega) \cos \phi_n(x, \omega) + b_n(\omega) \sin \phi_n(x, \omega)\}, \tag{A.3}$$

where

$$\phi_n(x, \omega) = \int_0^x J_n(\xi, \omega)\, d\xi, \tag{A.4}$$

$$a_n(\omega) = J_n^{1/2}(0, \omega), \tag{A.5}$$

and

$$\begin{aligned} b_n(\omega) = \{&J_n^{1/2}(1, \omega)\, J_n^{1/2}(0, \omega) \sin \phi_n(1, \omega) + \tfrac{1}{2}J_n'(1, \omega)\, J_n^{-3/2}(1, \omega)\, J_n^{1/2}(0, \omega) \cos \phi_n(1, \omega) \\ &- \rho_n^{-1}(1)\, \rho_n'(1)\, J_n^{-1/2}(1, \omega)\, J_n^{1/2}(0, \omega) \cos \phi_n(1, \omega)\}/ \\ &\{J_n^{1/2}(1, \omega) \cos \phi_n(1, \omega) - \tfrac{1}{2}J_n'(1, \omega)\, J_n^{-3/2}(1, \omega) \sin \phi_n(1, \omega) \\ &+ \tfrac{1}{2}\rho_n^{-1}(1)\, \rho_n'(1)\, J_n^{-1/2}(1, \omega) \sin \phi_n(1, \omega)\}. \end{aligned} \tag{A.6}$$

Then $\mathbf{p}_n(x, \omega) = v_n(x, \omega)\, \rho_n^{1/2}(x)$ is the asymptotic solution of Eq. (7) and it is used in the integrand of Eq. (9).

Appendix B

The propagation of a short acoustic pulse through the ocean layer with the density profile $\rho^*(x)$ is described by the solution of the following initial boundary value problem of the linear hyperbolic system,

$$\begin{aligned} \partial u/\partial t &= -\rho^{*-1}(x)\, \partial p/\partial x, & 0 < x < 1, \\ \partial p/\partial t &= -\partial u/\partial x, & 0 < t, \end{aligned} \tag{B.1}$$

with initial conditions

$$u(x, 0) = p(x, 0) = 0, \tag{B.2}$$

and boundary conditions

$$\begin{aligned} u(1, t) &= 0, \\ p(0, t) &= 100\{1 - \cos(200\pi t)\}, \qquad 0 \leqslant t \leqslant 0.01 \\ &= 0, \qquad\qquad\qquad\qquad t > 0.01. \end{aligned} \tag{B.3}$$

To damp put the stable numerical oscillations (Gibb's phenomenon) in the neighborhood where the solution has either a discontinuity or a steep gradient; an artificial viscosity term $\nu\partial^2 u/\partial x^2$ is added to the right-hand side of the first equation of Eq. (B.1) [28]. Along with it, an extra boundary condition, $\partial u/\partial x\,|_{x=0} = -20{,}000\pi \sin(200\pi t)$ for $0 \leqslant t \leqslant 0.01$ and 0 for $t > 0.01$ must be added to Eq. (B.3).

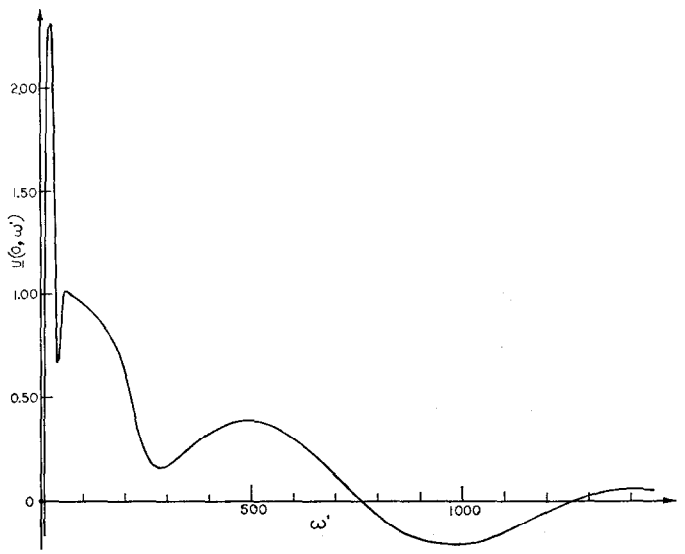

FIG. 16. Fourier cosine transform of $u(0, t)$ plotted as a function of ω'.

The above system is solved numerically by using a method which is based on the method of lines with the space variable x discretized by a finite element collocation scheme and the integration of time by the GEAR algorithm [29]. In particular, the Fourier cosine transform of $u(0, t)$ is computed by using a fast Fourier transform routine [30] and is plotted in Fig. 16. It is obvious that the low frequency spectrum contains more energy than the high frequency spectrum. If the pulse has longer duration, then this phenomenon will be even more pronounced.

ACKNOWLEDGMENT

This research has been supported in part by the Office of Naval Research under Contract N00014-76-C-0804.

REFERENCES

1. Y. M. CHEN AND J. SURMONT, *J. Math. Anal. Appl.* **46** (1974), 275–288.
2. Y. M. CHEN AND J. SURMONT, *Appl. Math. Comput.* **2** (1976), 197–228.
3. J. SURMONT AND Y. M. CHEN, *J. Comput. Phys.* **13** (1973), 288–302.
4. L. V. KANTOROVICH AND G. P. AKILOV, "Functional Analysis in Normed Spaces" (D. E. Brown, Tr.), Pergamon, Oxford, 1964.
5. G. BACKUS AND F. GILBERT, *Geophys. J. Roy. Astron. Soc.* **13** (1967), 247–276.
6. G. BACKUS AND F. GILBERT, *Geophys. J. Roy. Astron. Soc.* **16** (1968), 169–205.
7. G. BACKUS AND F. GILBERT, *Philos. Trans. Royal Soc. Ser. A* **266** (1970), 123–192.
8. A. N. TIHONOV, *Sov. Math. Dokl.* **4** (1963), 1035–1038.
9. A. ALBERT, "Regression and the Moore–Penrose Pseudoinverse," Academic Press, New York, 1972.
10. D. S. TSIEN AND Y. M. CHEN, A numerical method for nonlinear inverse problems in fluid dynamics, *in* "Computational Methods in Nonlinear Mechanics," Proc. International Conf. Comp. Methods in Nonlinear Mech., The University of Texas at Austin, Sept. 1974, pp. 935–943.
11. I. M. GELFAND AND B. M. LEVITAN, *Amer. Math. Soc. Transl. Ser. Z* **1** (1955), 253–304.
12. G. BORG, *Acta Math.* **78** (1946), 1–96.
13. M. G. KREIN, *Dokl. Akad. Nauk SSSR (N.S.)* **76** (1951), 21–24.
14. H. HOCHSTADT, *Acta Math.* **119** (1967), 173–192.
15. M. L. GERVER AND D. A. KAZDAN, *Mat. USSR-Sb.* **2** (1967), 199–206.
16. O. H. HALD, "On Discrete and Numerical Inverse Sturm–Liouville Problems," Ph.D. Thesis, New York University, New York, 1972.
17. V. BARCILON, *Geophys. J. Roy. Astron. Soc.* **38** (1974), 287–298.
18. V. BARCILON, *Z. Angew. Math. Phys.* **27** (1976), 347–358.
19. L. D. LANDAU AND E. M. LIFSHITZ, "Fluid Mechanics," Pergamon, London, 1959.
20. G. NEUMANN AND W. J. PIERSON, "Principles of Physical Oceanography," Prentice–Hall, Englewood Cliffs, N. J., 1966.
21. I. STAKGOLD, "Boundary Value Problems of Mathematical Physics," Vol. I, Macmillan, New York, 1967.
22. "The IMSL Library Reference Manual," ed. 4, International Mathematical and Statistical Libraries, Inc., 1975.
23. H. B. KELLER, "Numerical Methods for Two-Point Boundary-Value Problems," Blaisdell, Waltham, Mass., 1968.
24. C. W. GEAR, "Numerical Initial Value Problems in Ordinary Differential Equations," Prentice–Hall, Englewood Cliffs, N. J., 1971.
25. A. C. HINDMARSH, "GEAR: Ordinary Differential Equation System Solver," Lawrence Livermore Laboratory Rept. UCID-30001, Rev. 2, 1972.
26. P. M. MORSE AND H. FESHBACK, "Methods of Theoretical Physics," Part II, McGraw–Hill, New York, 1953.
27. G. S. S. AVILA AND J. B. KELLER, *Commun. Pure Appl. Math.* **16** (1963), 363–381.
28. R. D. RICHTMYER AND K. W. MORTON, "Difference Methods for Initial Value Problems," 2nd ed., Interscience, New York, 1967.
29. N. K. MADSEN AND R. F. SINCOVEC, General software for partial differental equations *in* "*Recent Developments in Numerical Methods for Differential Systems*" (W. E. Schiesser *et al.*, Eds.), Academic Press, New York, 1976.
30. R. C. SINGLETON, *IEEE Audio Electroacoust.*, **AU-17** (1969), 83–103.